
Article:
Terzioglu, F. orcid.org/0000-0002-2639-2992, Rongong, J. and Lord, C. (2023) Influence of particle sphericity on granular dampers operating in the bouncing bed motional phase. Journal of Sound and Vibration, 554. 117690. ISSN 0022-460X

https://doi.org/10.1016/j.jsv.2023.117690

Journal of Sound and Vibration 554 (2023) 117690

Contents lists available at ScienceDirect

Journal of Sound and Vibration

journal homepage: www.elsevier.com/locate/jsvi

Influence of particle sphericity on granular dampers operating in the bouncing bed motional phase

Furkan Terzioglu *, Jem Athing Rongong, Charles Eric Lord

Department of Mechanical Engineering, University of Sheffield, Mappin Street, Sheffield S1 3JD, UK

ARTICLE INFO

Keywords:
Particle damping
Granular bouncing bed
Non-spherical particle

ABSTRACT

This paper presents new research to determine the effect of particle shape on the energy dissipation in a granular damper operating in the bouncing bed motional phase. This is accomplished by conducting controlled experiments and validated Discrete Element Method (DEM) simulations for a broad collection of spheroidal particle shapes at vibration amplitudes of up to 50 g. The findings show that non-spherical particles significantly change the condition known as the "bouncing bed onset amplitude" which is the vibration amplitude at which granular damping is maximised. It is shown that the packing parameter known as the coordination number is an indicator of this change and that there is a correlation between the shear properties of the granular medium and the amplitude at which it delivers optimum energy dissipation. This paper also presents a sensitivity analysis specific to the bouncing bed phase which considers variations in particle modulus, density, restitution coefficient and friction. This shows that the observations about the effects of particle shape are valid over a broad range of conditions.

1. Introduction

A granular damper is simple to construct: the most basic design is an enclosure that is partially filled with small particles. A vibrating system can be damped by attaching such devices at suitable locations, which are usually in places where the vibration level is high. Within a damper, vibrational kinetic energy is transmitted to the particles from the enclosure walls *via* momentum exchange. The main mechanisms for energy dissipation are inelastic collisions and friction, as particles interact with each other and the enclosure walls. In general, granular dampers are passive systems that can provide low cost, mass-efficient damping without significantly altering the stiffness of a structure whilst operating under extreme environmental conditions [1]. As a result, their deployment in practical noise and vibration control applications has received considerable attention in recent years [2–6].

While they can be highly effective, granular dampers exhibit complex, amplitude-dependent characteristics. To explain this behaviour, and thereby develop reliable designs, numerous experimental and theoretical studies have been carried out as summarised in recent review articles [7,8]. Amplitude-dependent nonlinearity has been noted when considering the free vibration response of a beam enriched with a granular damper [9,10]. Nonlinearity has also been reported as amplitude-dependent modal damping parameters obtained from the frequency response functions of a structure with an attached granular damper [11,12]. However, in order to gain a better understanding of granular damping mechanisms, structure-independent granular damping evaluation has been the subject of several studies [13–16]. In this approach, the damper performance is evaluated without attaching it to a host structure. This

* Corresponding author.
E-mail address: fterzioglu1@sheffield.ac.uk (F. Terzioglu).

https://doi.org/10.1016/j.jsv.2023.117690
Received 7 November 2022; Received in revised form 6 March 2023; Accepted 28 March 2023
Available online 29 March 2023

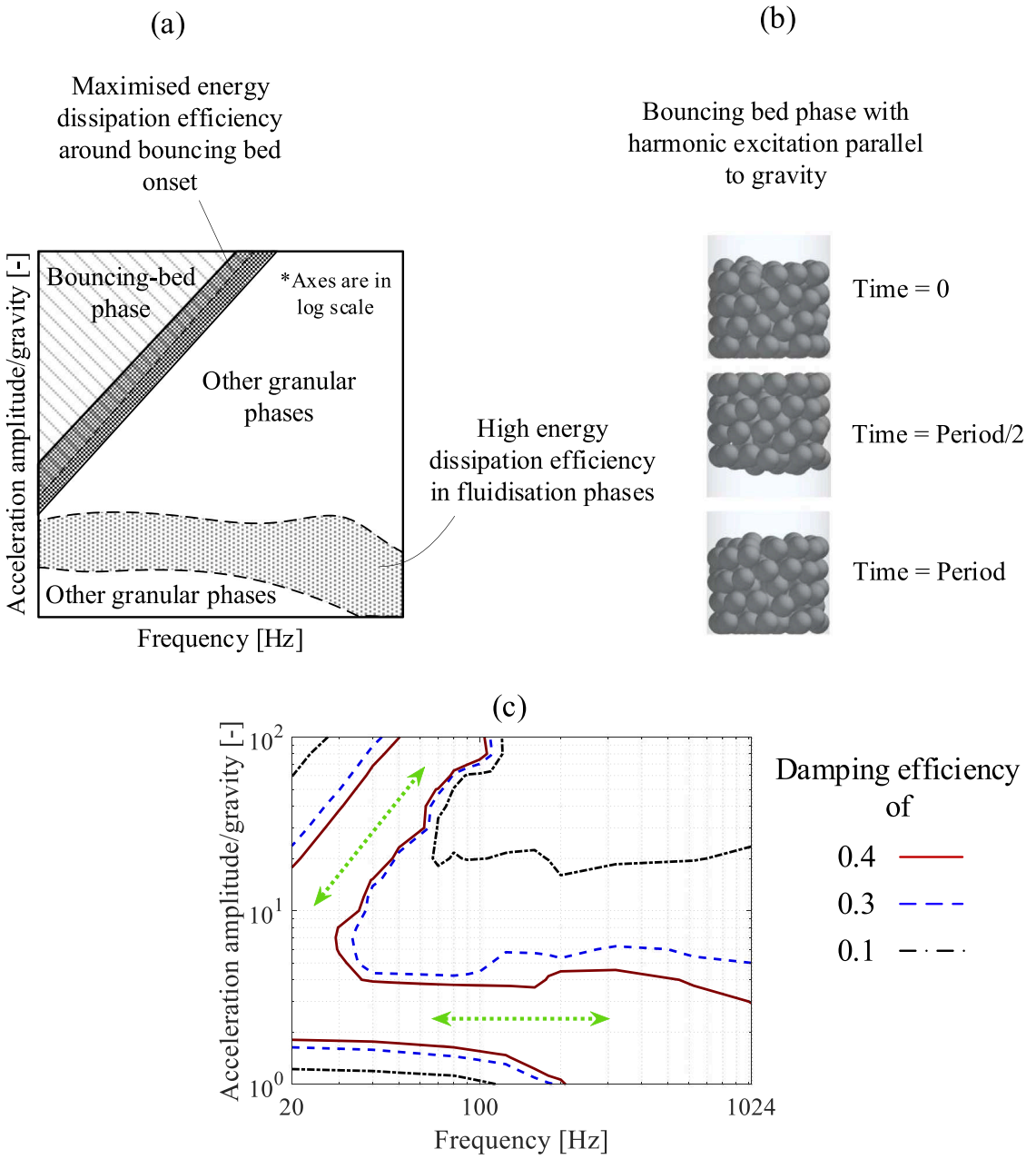

Fig. 1. The bouncing bed motional phase where (a) shows its location on a granular phase map, (b) shows particle movement within the case and (c) is a typical damping efficiency map available in the literature [25].

results in much better control of the vibration environment that the damper is subjected to. An important finding from this type of study is that there is an indisputable relationship between type of collective motion displayed by vibrated granules and the associated energy dissipation performance [17]. This is because the type of collective motion determines the prevalence, magnitude, direction and timing of inter-particle and particle-enclosure interactions. This can result in dramatic differences in the exhibited amplitude-dependent energy dissipation effectiveness that arises when different collective motion types are observed [18,19].

The type of motional behaviour in a vibrated granular medium is usually identified by making observations from experiments and simulations. As observed motion types vary depending on vibration amplitude and frequency, their distribution can be presented efficiently as a motional phase map in an amplitude-frequency plane [20,21].

Apart from vibration amplitude and frequency, granular motion is also sensitive to several factors such as the volume filling ratio, the existence or lack of gravity and the vibration-to-gravity directional orientation. Thus, recently, granular damping studies have started to focus on assessing the relationships between motion type (sometimes called the 'granular motion phase') and energy

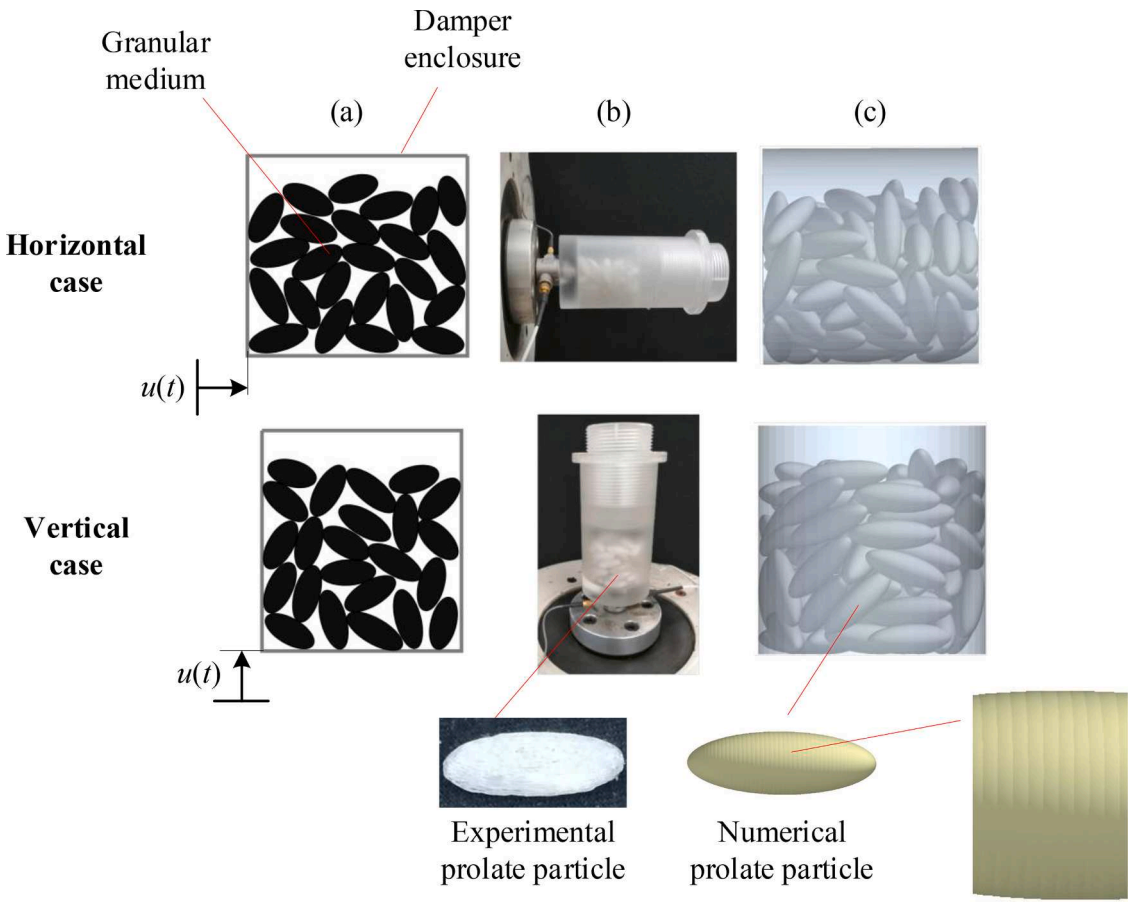

Fig. 2. A granular damper containing prolate spheroid particles under two different vibration-to-gravity orientations, (a) conceptual, (b) experimental and (c) numerical models.

dissipation behaviour [22–25]. Both numerical and experimental studies have shown that maximised granular damping can be achieved at the onset of the 'bouncing bed' phase where the particles move as an aggregated mass that periodically impacts both ends of the enclosure [18,19,24,25]. This is analogous to optimum performance in a single-particle impact damper where two equally spaced impacts per cycle have been shown to be the most effective [26].

An example of a phase map that identifies the bouncing bed motional behaviour is presented in Fig. 1(a) while Fig. 1(b) shows the way in which the particles move within the cavity during this phase. The fact that the phase map schematically shows the most effective granular energy dissipation zones can be verified by comparing it with Fig. 1(c) which shows the energy dissipation effectiveness of a particular granular damper [25]. Double-sided green arrows are placed in the regions of high damping efficiency to help the reader to identify the ridges associated with the bouncing bed and fluidisation phases.

The effects of particle mass, particle size, particle filling ratio, enclosure shape, enclosure dimensions and material properties have been extensively studied to maximise granular energy dissipation performance [11,27–29]. However, what is not yet clear is the influence that particle shape can have on granular energy dissipation behaviour since there have been only few quantitative analyses on non-spherical particles [30–33]. Sanchez et al. [30] investigated two-dimensional triangle, square and hexagon shapes while Pourtavakoli et al. [32] examined a range of non-spherical particle shapes constructed by agglomerations of spheres. Both systematic studies were performed solely using the Discrete Element Method (DEM) simulations and the obtained results are specific to the unusual shapes investigated. However, it is evident from the existing studies (and obvious when considering local granular packing) that particle shape affects contact conditions and particle mobility within the granular medium. As these factors directly affect the dominant granular motional phase that is present when the damper is subjected to specific excitation conditions [33], it is reasonable to assume that changes in particle shape may have a significant impact on energy dissipation.

The aim of this work is to investigate the energy dissipation performance of a granular damper containing non-spherical particles operating in its most efficient motional phase, namely the bouncing bed. To enable a systematic study, spheroidal particles with a range of aspect ratios (both oblate and prolate) are considered. Excitation is supplied both parallel and perpendicular to gravity. Because sensitivity to frequency in the bouncing bed phase can be inferred from sensitivity to amplitude [25], trends associated with particle shape are identified over a large number of amplitude levels but only two different frequencies.

Table 1
Material and physical model properties.

Parameters	
Young's modulus	3.3 GPa
Poisson's ratio	0.37
Density	1190 kg/m^3
Enclosure diameter	0.04 m
Enclosure height	0.04 m
Enclosure mass	0.151 kg
Enclosure first mode	>1200 Hz
Reference sphere diameter	7.56 mm
Number of particles	90
Coefficient of restitution	0.86
Coefficient of friction	0.52

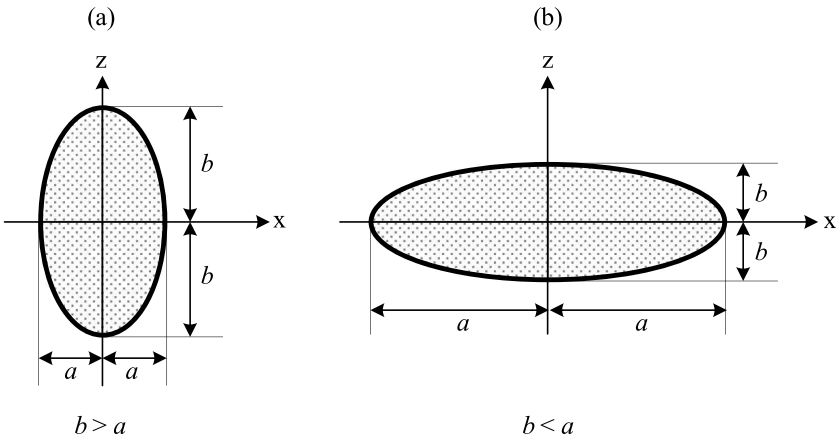

Fig. 3. Ellipses from which (a) oblate and (b) prolate spheroids were generated by rotation around the x-axis.

2. Methodology

2.1. Granular damper configuration

The damper considered in this work comprised a cylindrical enclosure containing a fixed number of nominally identical particles. The structure-independent approach was employed to obtain the dissipated energy under steady-state conditions using both experimental and numerical techniques. This approach was selected to allow comparisons to be made over different frequency and amplitude ranges. Sketches of the configuration are provided in Fig. 2(a), images of the experiment are shown in Fig. 2(b) and the equivalent numerical DEM representations are given in Fig. 2(c).

In order to understand the effects of vibration direction on performance, the damper was studied with excitation both perpendicular to the direction of gravity and parallel to it. For convenience, the terms "horizontal" and "vertical" are used to reflect this, as indicated in Fig. 2. For both loading directions, the motion of enclosure $u(t)$ is defined as:

$$u(t) = \frac{\Gamma g}{\omega^2}\sin(\omega t) \tag{1}$$

where, g is the gravitational acceleration constant; ω is the excitation frequency; and t stands for the time. Γ is the non-dimensional acceleration amplitude, defined as the amplitude of acceleration experienced by the damper enclosure divided by the acceleration due to gravity.

Important parameters describing the damper configuration are listed in Table 1. The enclosure size, particle size and number of particles were selected so that it would be relatively easy to observe the bouncing bed phase. An acrylic-type polymer was selected for the enclosure and particles for the following reasons:

i. to simplify manufacturing processes for the physical specimens,
ii. to eliminate magnetic interaction forces,
iii. to prevent local plastic deformations,
iv. to avoid excessive inertial forces (which are particularly large in the bouncing bed phase) and,
v. to reduce simulation times by increasing the minimum time step through the use of a material with a low wave speed.

Table 2
Created particle types for experiments and simulations.

Aspect ratio	Experimental	DEM: multi-sphere
0.70	+	–
0.85	+	–
1.00	+	+
1.25	–	+
1.50	+	+
2.00	+	+
2.50	–	+
3.00	+	+

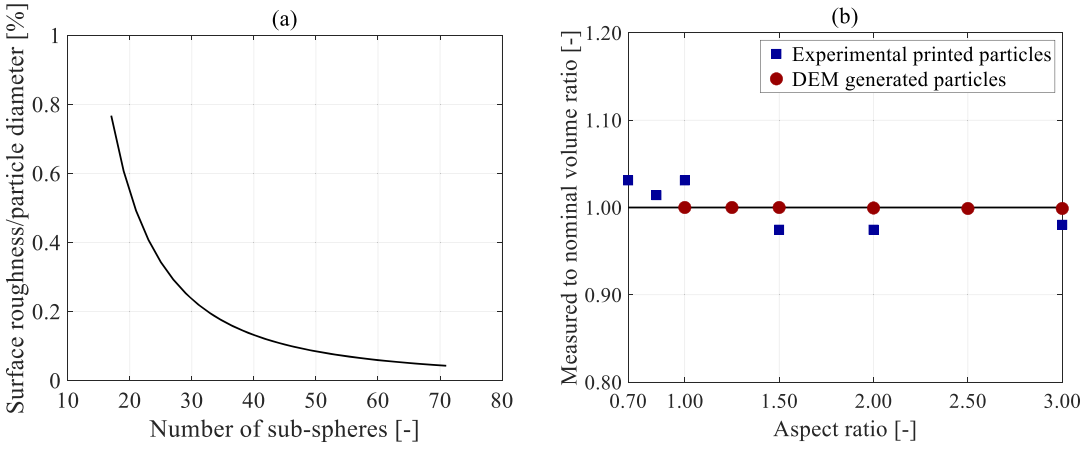

Fig. 4. Shape imperfections in particles with (a) the relative surface roughness of a multi-sphere particle with α = 3.00 and (b) the volume deviation with respect to a perfect sphere.

The contact properties for the acrylic material, namely the coefficients of restitution and friction for both particle-particle and particle-enclosure contacts shown in Table 1, were estimated from the work of Saeki on similar particles [34,35]. The uncertainty introduced by this estimation was investigated numerically to understand the sensitivity of the result to possible differences between the materials used in this work and in the referenced articles.

2.2. Spheroidal particle shapes

A spheroid is generated by revolving an ellipse around one of its principal axes. Referring to the ellipses shown in Fig. 3, it can be seen that the shape is defined by the aspect ratio, $\alpha = a/b$. When $a < b$, the particle is flattened (or oblate) whereas $a > b$ results in an elongated (or prolate) shape. In a perfect sphere, $a = b$.

The effects of particle shape were investigated using collections of identical particles possessing an aspect ratio in the range of 0.70 to 3.00. To simplify comparison, the mass and number of particles was kept constant. This required particles to have the same volume, irrespective of aspect ratio. The particle dimensions were then defined in terms of the reference perfect sphere radius, r_{sphere}, and the aspect ratio.

$$\begin{aligned} b &= \alpha^{-1/3} r_{\text{sphere}} \\ a &= \alpha b \end{aligned} \tag{2}$$

In this paper, the granular dampers were studied experimentally and numerically to provide a parallel investigation. The numerical study was used to improve observation of the motion of individual particles under different excitation conditions and to allow sensitivity analyses to be conducted one parameter at a time.

The calculation steps of DEM such as contact detection and contact force-deformation modelling have been thoroughly tested and shown to be simple, efficient, and accurate for perfect spheres. In this study, for non-spherical particles, the multi-sphere approach was utilised to maintain the same computational procedure as for perfect spheres. In this approach, a non-spherical particle shape is created using a number of inter-penetrating, perfect spheres. Increasing the number of sub-spheres generally increases the accuracy of the represented shape but also increases the computational effort when running the subsequent DEM solutions. The multi-sphere approach has been tested, implemented and reliably used in a number of different studies [36–38].

Numerical analyses were conducted for six different particle shapes (5 prolate spheroids and 1 perfect sphere) as shown in Table 2. The analytical method developed by Markauskas et al. [39] was implemented to generate the prolate spheroid particles. This efficient

method allows explicit determination of the relative positions of each sub-sphere by iteratively solving a set of equations. For oblate particles however, such an analytical method does not exist. Although there are some optimisation-based tools which locate sub-spheres in a given non-spherical particle geometry [40,41], the optimisation approach produced relatively large shape inconsistencies (in the form of surface ridges and troughs) when generating oblate particles. These surface defects in the numerically generated particles were considered large enough to alter results so the investigation of oblate particles was limited to experiments.

Because the analytical method provides a regular sub-sphere chain along an axis, i.e., the local x-axis according to Fig. 3(b), increasing number of sub-spheres yields smoother and more accurate representation of a prolate spheroid. However, as this also increases computational requirements, there is usually a practical limit on the number of sub-spheres used. In this work, the minimum required number of sub-spheres was estimated by considering the surface roughness caused by the multi-sphere approach for the particle with the highest aspect ratio, where $\alpha = 3.00$. The roughness was estimated using the mean height of the ripples formed by the sub-spheres, which can be seen in Fig. 2(c). The curve in Fig. 4(a) shows how the surface roughness is reduced when the number of sub-spheres is increased. Experimental work has suggested that the effect of surface roughness on granular energy dissipation becomes insignificant when roughness is below approximately 0.2% of the particle size [42]. In this work, to be well below this level, 51 sub-spheres were used for each numerical prolate particle (roughness around 0.04%). This provided a reasonable compromise between minimising the error of the represented shapes and the computational load in the DEM solutions. It has been verified elsewhere that the use of such numbers of sub-spheres results in an excellent representation of smooth prolate spheroids (with maximum aspect ratio of 3.00) for numerical simulations [39]. It can be seen from Fig. 4(b), the numerically created prolate particles are close in size to the exact shapes.

For the experimental investigations, six different particle types were produced using 3D printing, as indicated in Table 2. (Intermediate aspect ratios of $\alpha = 1.25$ and 2.50 were added to the study to provide additional detail, but due to the close match between experimental and numerical results for all other shapes, manufacture of specimens with these aspect ratios was considered unnecessary, hence only simulation results are available for these shapes). The manufacturing process generated some surface defects which can be seen in Fig. 2. However, as shown in Fig. 4(b), these defects did not affect the volume consistency significantly, with the error being typically below 2%. Additionally, in order to verify that the sphericity did not deviate significantly from the intended particle shape, surface roughness measurements were carried out on an oblate particle ($\alpha = 0.70$). The most severe roughness was measured on paths perpendicular to the printed ridges on the particle surface. These had an average roughness of 11.32 μm which was considered small in comparison to the particle diameter (< 0.2%).

2.3. Quantification of granular energy dissipation

With the structure-independent approach, it is not possible to extract the structural effective mass and therefore the maximum stored energy needed in the classical loss factor definition. Instead, the damping efficiency parameter was used. This is defined as the ratio of energy dissipated over a vibration cycle, $\widetilde{E}_{\text{dissipated}}$, to the maximum achievable energy dissipated in a vibration period, $\widetilde{E}^{\max}_{\text{dissipated}}$.

$$\text{Damping Efficiency} = \widetilde{E}_{\text{dissipated}} \Big/ \widetilde{E}^{\max}_{\text{dissipated}} \tag{3}$$

Using this measure, it was possible to compare energy dissipation performance in a consistent manner for different particle shapes and excitation conditions.

The maximum achievable energy dissipated by a vibrated granular medium has been expressed differently by several authors [18,43,44]. However, their derived energy expressions only differ from each other by a constant scaling term. The selected expression was that provided by Sack et al. [18] in which all particles undergo collective and completely inelastic collisions with an end wall of the cavity at precisely the time that the enclosure reaches its maximum velocity. These collisions occur twice per cycle, and the energy dissipated per cycle is,

$$\widetilde{E}^{\max}_{\text{dissipated}} = 4\left(\frac{\Gamma g}{\omega}\right)^2 \text{M}_{\text{particle}} \tag{4}$$

where, $\text{M}_{\text{particle}}$ is the total mass of particles in the enclosure.

Even in nominally steady-state conditions, dissipated energy can differ from one vibration period to another due to the complex non-linearities in granular damping. To obtain a reliable estimate, the approach taken for both numerical and experimental work was to estimate the average dissipated power ($P_{\text{dissipated}}$) over many cycles. The average energy dissipation per cycle was then obtained using:

$$\widetilde{E}_{\text{dissipated}} = 2\pi P_{\text{dissipated}} \big/ \omega \tag{5}$$

2.4. Experimental setup

The equipment used to identify the power dissipated by the granular damper is illustrated in Fig. 5. This test setup was originally introduced by Yang [13] and has since been used widely for this purpose. Testing involved sending excitation signals from the personal computer (PC) to the electromagnetic shaker *via* the digital analogue converter in the oscilloscope and the power amplifier. Signals

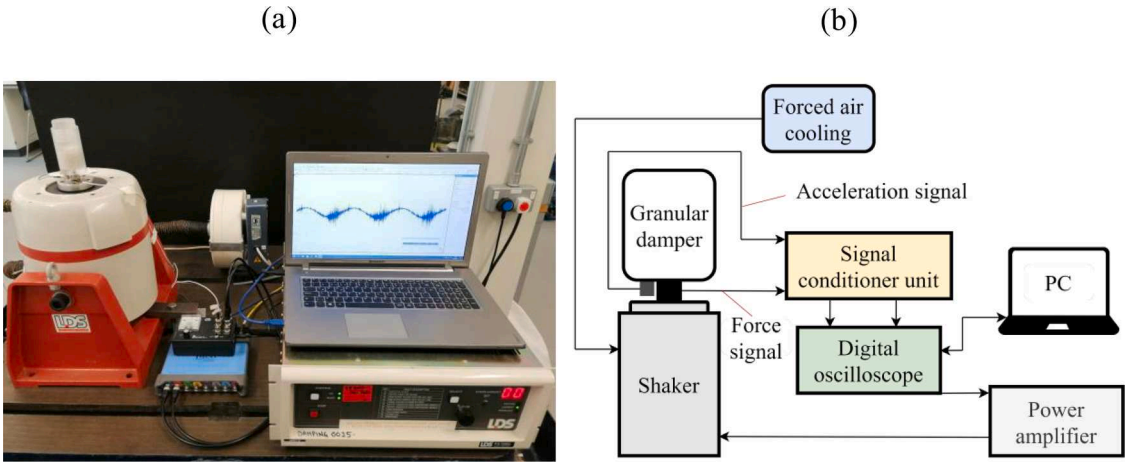

Fig. 5. Experimental test setup: (a) image and (b) schematic representation.

from the acceleration and force transducers were conditioned by the signal conditioner unit and captured by the digital oscilloscope to store in the PC for further processing.

The enclosure was manufactured using a transparent material to allow particle movement to be observed. To assemble this enclosure on the shaker, three important connections were involved: shaker-force transducer, force transducer-enclosure and enclosure-enclosure lid. Each of these connections had to be properly engaged before conducting measurements to ensure consistent rigidity. In this way, the initial phase angle error between the transducers arising from non-perfect connection was kept below 0.3% over the excitation ranges investigated.

At the start of each test, particles were allowed to settle inside the enclosure under the effect of gravity. Harmonic excitation, $u(t)$ was then given to the enclosure at the specified amplitude and frequency. After reaching steady-state regime, acceleration $\mathrm{a}(t)$ and force $\mathrm{f}(t)$ signals were recorded for 5 s using a sampling rate of 40 kHz.

The average dissipated power was calculated from the complex frequency-domain expressions for force and velocity. These were obtained from the captured time-domain acceleration and force signals using the discrete Fourier transform.

$$\mathbf{V}_k = \frac{1}{j\omega_k}\sum_{i=0}^{N-1}\mathrm{a}(t_i)e^{-j2\pi ki/N} \tag{6}$$

$$\mathbf{F}_k = \sum_{i=0}^{N-1}\mathrm{f}(t_i)e^{-j2\pi ki/N} \tag{7}$$

Here, ω_k is the discretised frequency determined by the signal length and the sampling frequency where $k = 0, 1, 2, \ldots, N\text{-}1$; N is the total number of data points in a single measurement; j is the imaginary number. The total complex power $\mathbf{P}^{\text{experimental}}$ can be calculated as the product of the complex force $\mathbf{F}_k$ and the complex conjugate velocity $\mathbf{V}_k{}^*$ over the whole frequency range as given below.

$$\mathbf{P}^{\text{experimental}} = \sum_{k=0}^{N-1}\frac{1}{2}\mathbf{F}_k\mathbf{V}_k^* \tag{8}$$

The real part of this complex power yields the average power dissipated by the granular damper. Alternatively, it can be obtained using the phase angles of the complex force $\varphi_{\mathbf{F}k}$ and the velocity $\varphi_{\mathbf{V}k}$ as shown in the following equation.

$$P_{\text{dissipated}}^{\text{experimental}} = \text{real}\left(\mathbf{P}^{\text{experimental}}\right) = \sum_{k=1}^{N-1}\frac{1}{2}|\mathbf{F}_k||\mathbf{V}_k|\cos\left(\varphi_{\mathbf{F}_k} - \varphi_{\mathbf{V}_k}\right) \tag{9}$$

2.5. Numerical method

Numerical assemblies of particles within an enclosure (as shown in Fig. 2(c)) were constructed, excited, and analysed using DEM. The theory of DEM was first introduced by Cundall and Strack [45], and has been found useful for granular damping simulations [15,22,28,35,46]. It allows each particle to be modelled as an unconstrained rigid body for which the translational and rotational motions within the enclosure are evaluated simultaneously solving the Newton–Euler equations of motion at appropriately small time-steps. For a single time-step, the equations of motion are constructed for each particle by establishing the gravitational load and the contact forces between interreacting bodies. A commercial three-dimensional DEM algorithm [41] was utilised to carry out the numerical simulations of granular dampers and obtain the dissipated power.

As the multi-sphere approach was employed to generate non-spherical particles, the resulting contact forces were computed using

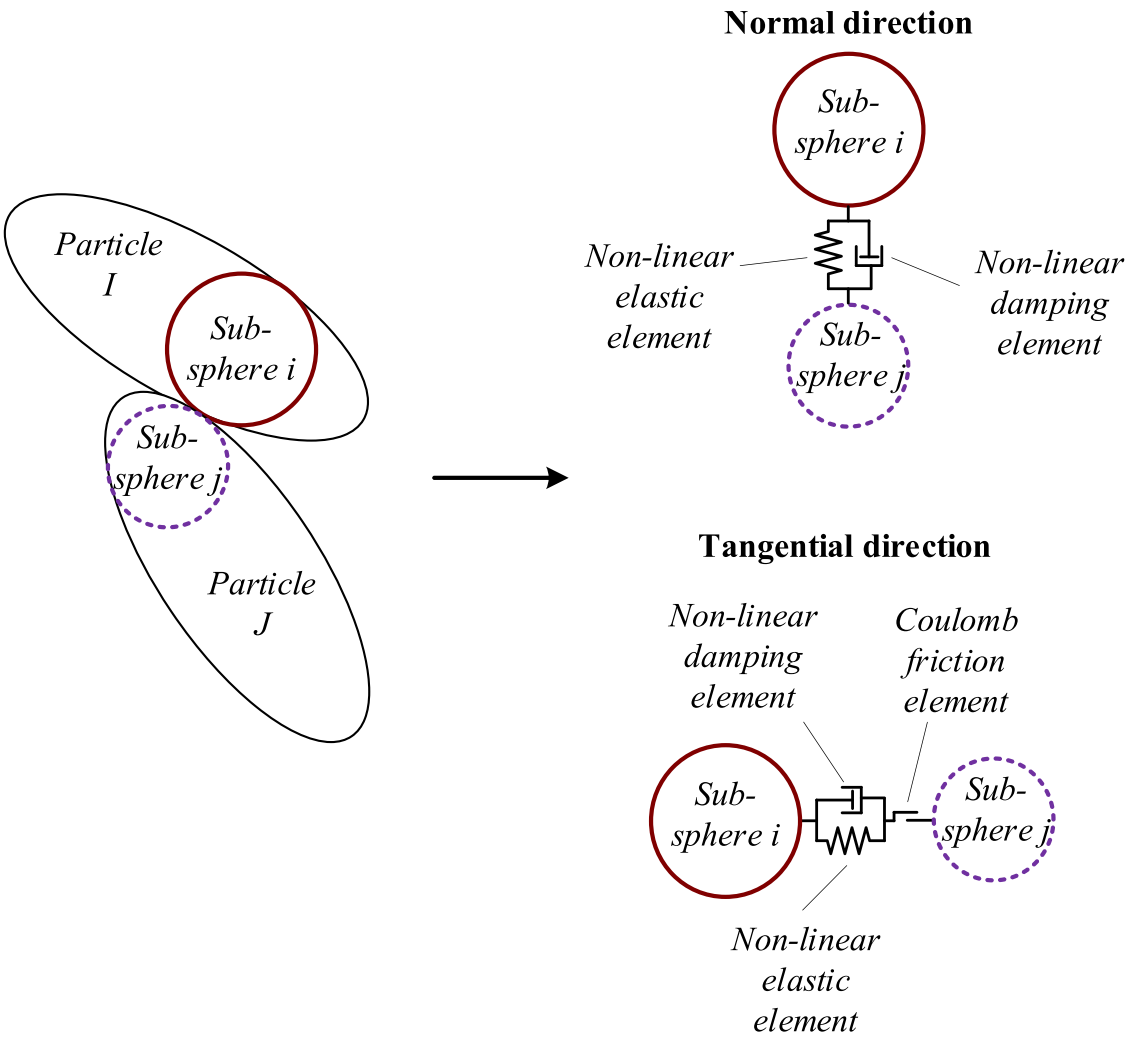

Fig. 6. Particle contact model.

spherical contact force-deformation relationships at each contact point identified. This is illustrated in Fig. 6 using two interacting prolate spheroid particles. The elastic behaviours of the contact model were based on the non-linear Hertz theory in the normal direction and the non-linear Mindlin–Deresiewicz approach in the tangential direction [47–51]. In order to limit the tangential force and represent frictional dissipation, a Coulomb friction element was included. The non-linear dissipative force proposed by Tsuji et al. [52] was used in the contact model to account for inelasticity of particles.

For the total simulation time, 18 vibration periods were used in addition to an initial 0.2 s during which the particles were allowed to settle inside the enclosure under the effect of gravity. The dissipated power was subsequently calculated using results from the last 15 cycles because in the bouncing bed mode, nominally steady-state behaviour was reached after the first 3 cycles. Setting the start and finish times as t_1 and t_2, the expression for dissipated power is:

$$P_{\text{dissipated}}^{\text{numerical}} = \frac{E_{\text{cumulative}}(t = t_2) - E_{\text{cumulative}}(t = t_1)}{t_2 - t_1} \tag{10}$$

where, $E_{\text{cumulative}}$ is the cumulative dissipated energy by the damper.

Since the dynamic particle motions were determined using a time marching approach in DEM simulations, the dissipated energy was computed employing an incremental scheme as well. The total dissipated energy, $E_{\text{cumulative}}(t)$ was cumulatively evaluated using results from each previous time increment, for which the dissipated energy is given by:

$$\Delta E_{\text{dissipated}} = \sum_{I=1}^{N_{\text{particle}}} \sum_{i=1}^{N_{\text{sub-sphere},I}} \sum_{J=1}^{N_{\text{contact},Ii}} \sum_{j=1}^{N_{\text{contact},IiJ}} \int_{T_{\text{contact},IiJj}} \left\{ \left| \mathbf{F}_{IiJj}^{nd} \cdot \mathbf{v}_{IiJj}^{n} \right| + \left| \mathbf{F}_{IiJj}^{td} \cdot \mathbf{v}_{IiJj}^{t} \right| \right\} dt \tag{11}$$

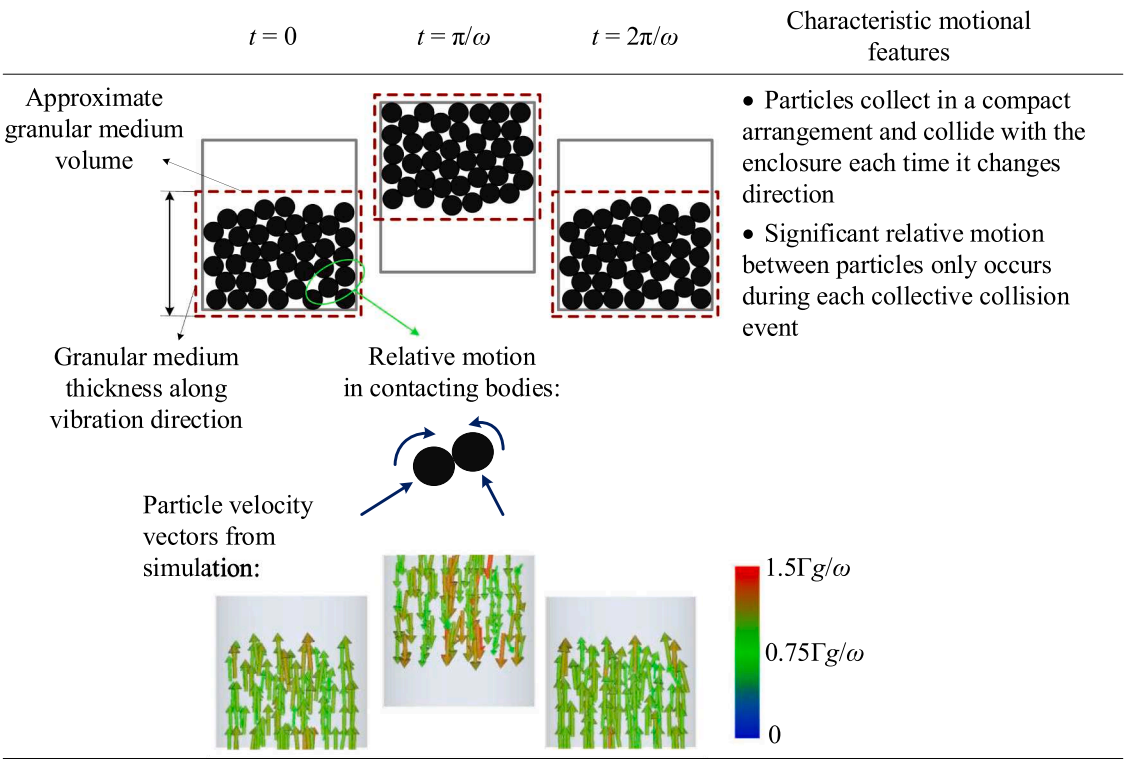

Fig. 7. Illustrations and features of the bouncing bed granular motional phase.

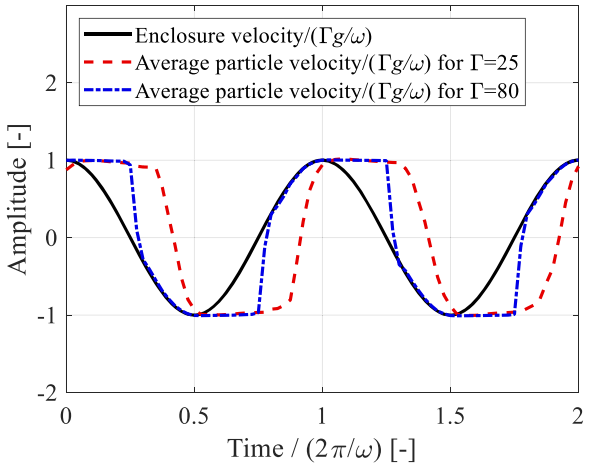

Fig. 8. Normalised velocity histories of a simulated granular damper with particles of $\alpha = 1.00$ for horizontal 40 Hz excitation.

where, $T_{\text{contact},IiJj}$ is the duration of contact between the sub-sphere i of the particle I and the sub-sphere j of the particle J; $\mathbf{F}^{nd}_{IiJj}$ and $\mathbf{F}^{td}_{IiJj}$ are the dissipative forces along normal and tangential directions, respectively; $\mathbf{v}^{nd}_{IiJj}$ and $\mathbf{v}^{td}_{IiJj}$ are the relative velocities along the corresponding directions; $N_{\text{contact},IiJ}$ is the number of contacts that the sub-sphere i of the particle I has with the sub-spheres of particle J; $N_{\text{contact},Ii}$ is the number of contacts that the particle I has with the other particles; $N_{\text{sub-sphere},I}$ is the number of sub-spheres that construct the particle I; and N_{particle} is the number of particles in the simulated model.

3. Dissipative properties of a granular medium in the bouncing bed phase

In a granular damper, if the vibration intensity is sufficiently strong, the particles collectively produce periodic impacts with both end boundaries of the enclosure in a single vibration cycle. This motional behaviour is known as the bouncing bed phase. Although this term is sometimes used to describe collisions with only one wall of the enclosure [20], in this study it is only used to describe two-sided

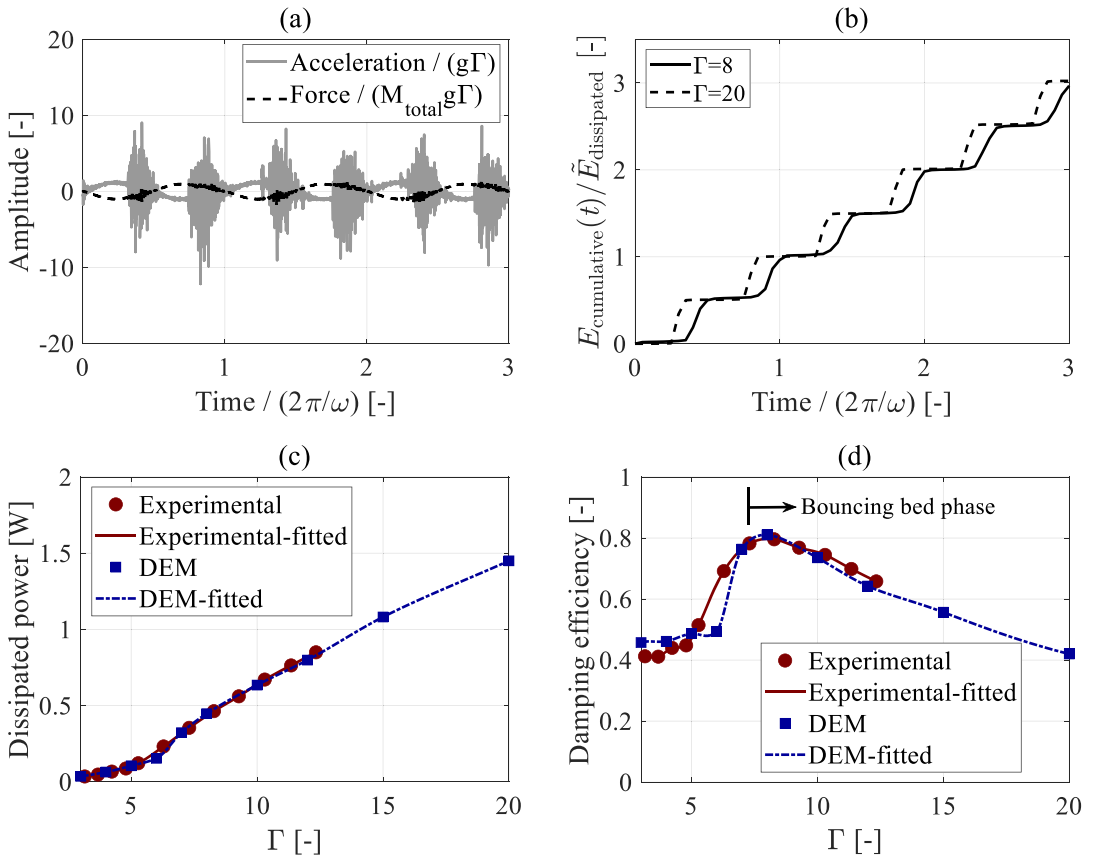

Fig. 9. Results for a damper with particles of aspect ratio $\alpha = 3.00$ for horizontal 20 Hz excitation: (a) time signals from experiments for $\Gamma = 10$, (b) steady-state cumulative dissipated energy histories from simulations, (c) experimental and numerical dissipated powers, (d) damping efficiency obtained from the dissipated powers presented in (c).

periodic collisions. A description of this motional phase is provided in Fig. 7.

When a damper is operating in the bouncing bed mode, most energy dissipation occurs during the collective collisions. It is therefore reasonable to assume that the relative velocity between the enclosure and the particle collection directly before and during a collision is an important factor affecting the amount of energy dissipated. To understand this better, it is useful to study the evolution of particle mean velocity against time when operating in the bouncing bed mode. Fig. 8 shows a comparison between the normalised mean velocities of the particles and the casing. Two vibration intensities within the bouncing bed phase are considered: $\Gamma = 25$ which is close to the bouncing bed onset where dissipation efficiency is high (refer to Fig. 1) and $\Gamma = 80$ where the dissipation efficiency is much lower. As the excitation direction is horizontal, change in particle velocity is only achieved during a collision event, and this ceases as soon as the casing decelerates.

Observation of particles undergoing these motions indicate that deformation of the particle bed, and hence energy dissipation, occurs during the collision event but only while the particles move relative to the casing. Fig. 8 shows that for high dissipation efficiency ($\Gamma = 25$), the collision starts when the particles are moving in the opposite direction to the enclosure with almost the same speed. At the higher vibration level ($\Gamma = 80$), the collision commences earlier in the cycle when the enclosure is almost at rest. The initial deceleration of the particles increases with vibration amplitude although once the particles reach the velocity of the enclosure, they move with it. The rapid initial deceleration can be attributed to tighter packing of the granular medium leading to an increase in its stiffness. The looser packing (and lower stiffness) occurring at $\Gamma = 25$ appears to provide more effective energy dissipation. It should be noted that this observation in the bouncing bed phase is valid at any excitation frequency or for any particle shape.

The initiation of the bouncing bed phase can be estimated using a simple relationship involving the excitation intensity (amplitude and frequency) and the clearance (distance the particles can travel) within the enclosure [18,19,24]. This can be written as,

$$\Gamma_{\text{optimum}} = \omega^2 h / g\pi \tag{12}$$

where, h is the clearance which, for spherical particles, can be estimated from the volume fill ratio v and the maximum achievable volume fill ratio $v_{\max}$ using,

$$h = L(1 - v / v_{\max}) \tag{13}$$

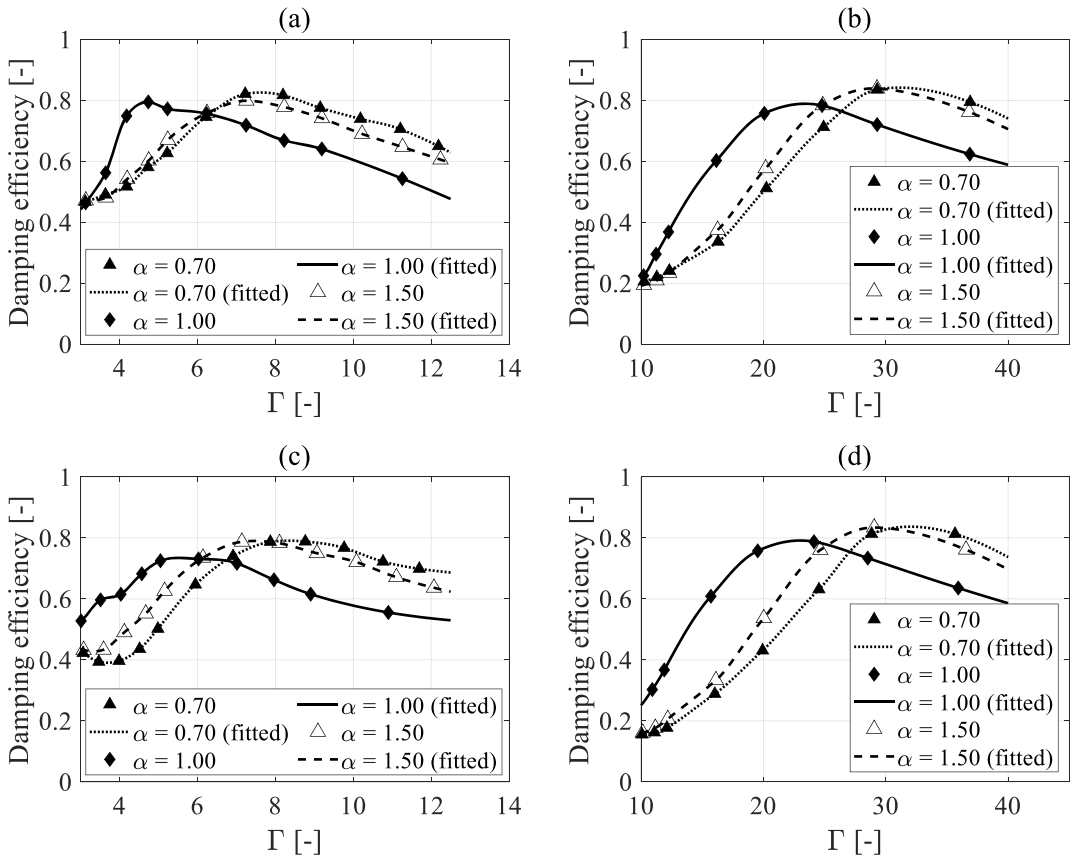

Fig. 10. Effect of particle shape on experimentally measured damping efficiency: (a) horizontal – 20 Hz, (b) horizontal – 40 Hz, (c) vertical – 20 Hz, (d) vertical – 40 Hz.

with v_{max} being in the range 0.55 to 0.64 depending on packing achieved. Note that L is the length of enclosure.

In this work, results were obtained at two different excitation frequencies. Estimating the clearance from the information in Table 1, the bouncing bed onset amplitudes were determined as approximately $\Gamma = 5$–7 at 20 Hz and $\Gamma = 20$–30 at 40 Hz for both vibration-to-gravity orientations. The intention was to map the excitation amplitude range $\Gamma = 1$ to 100. However, for the experiments, the vibration amplitude range had to be limited such as $\Gamma \leq 12.5$ for 20 Hz and $\Gamma \leq 40$ for 40 Hz due to the peak-to-peak displacement limitation of shaker.

While running experiments, it was noted that the bouncing bed phase can also be identified by observing the transducer signals. Examples of typical transducer signals are shown in Fig. 9(a). Here, the axes have been normalised and M_{total} is the sum of the enclosure mass and the particles. As this plot indicates, the periodic collective collisions are so intense that they cause significant distortions to the measured signals, particularly, the acceleration signal. Such intense collisions transfer a large portion of the vibrational energy to the particles and dissipate this transmitted energy through the interactions amongst the particles in a relatively short time. As a result, the cumulative energy dissipation history resembles a staircase, as can be seen in Fig. 9(b) for two different excitation amplitudes. It can be seen that at higher amplitude, each collision occurs earlier in the cycle and energy is dissipated over a shorter time period. Note that $\widetilde{E}_{dissipated}$ used for the normalisation in Fig. 9(b) is described by Eq. (5).

Fig. 9(c) provides a comparison of experimental and numerical dissipated powers obtained for prolate particles with $\alpha = 3.00$. Lines between data points were generated using piecewise cubic spline interpolation and added to allow better visualisation of the trends. It can be seen that experiments and simulations are well-correlated for all vibration amplitudes considered. Both sets of results display a clear increase in gradient around $\Gamma = 5$–7 which corresponds to the onset of the bouncing bed phase.

Fig. 9(d) shows the damping efficiency obtained for the power traces shown in Fig. 9(c). It can be seen that damping efficiency is highest around the bouncing bed onset amplitude, as has been noted in previous studies [9,10,18,19,24,27,53]. Increases in amplitude beyond the optimum result in gradually decreasing damping efficiency. This occurs because the dissipated power increases with amplitude at a slower rate than the maximum achievable level defined in Eq. (4). It is important to note that the shape of the damping efficiency curve is asymmetric: the rise in efficiency at low amplitude as the bouncing bed develops is much sharper than the decrease at high amplitude. This suggests that a design that locates the operating amplitude above the optimum will be more robust to uncertainty.

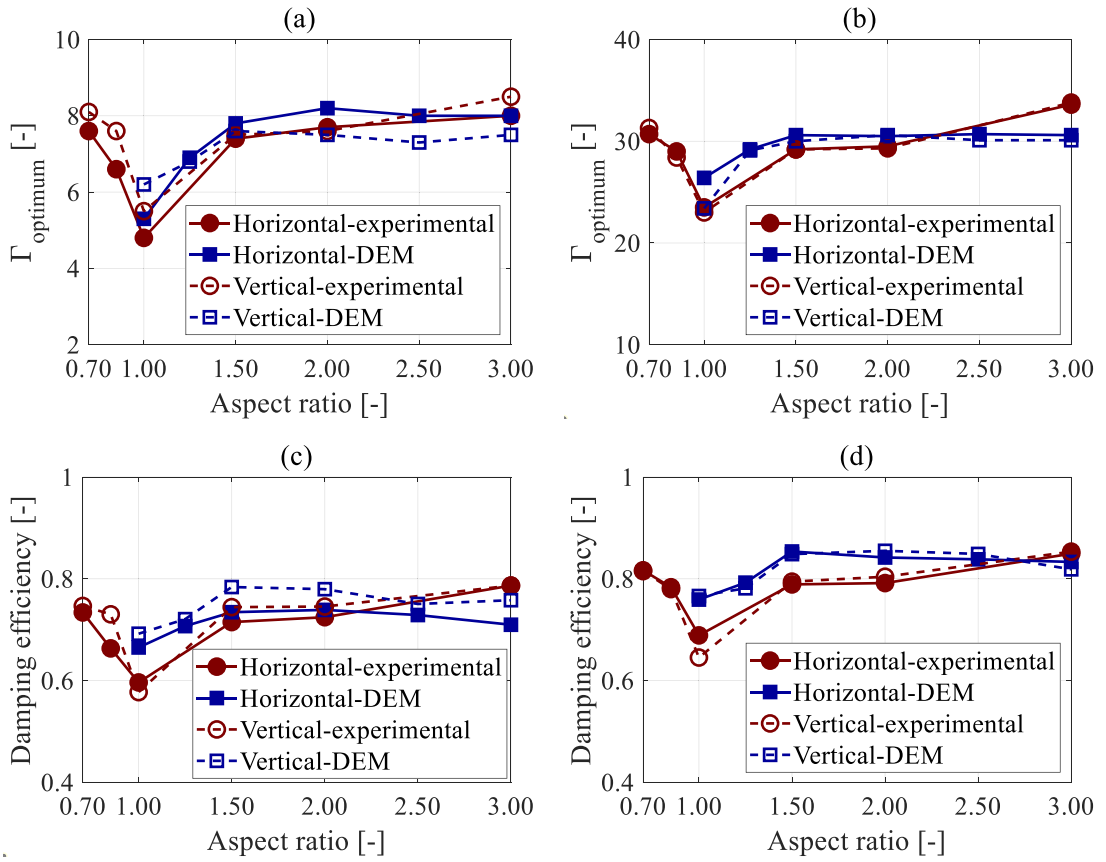

Fig. 11. Particle shape dependence in the bouncing bed phase: (a) onset amplitude variation at 20 Hz, (b) onset amplitude variation at 40 Hz, (c) damping efficiency variation at 20 Hz for $\Gamma = 10$ and (d) damping efficiency variation at 40 Hz for $\Gamma = 35$.

For each particle shape and condition, test and simulation runs were repeated three times to highlight any sensitivity to the starting arrangement of the particles and the significance of other random errors. Results showed that repeatability was high. For example, in the horizontal excitation case at 20 Hz, the deviation between damping efficiency levels for the same particle shape was lower than 2% for experiments and 4% in simulations. As a result, it was concluded that the energy dissipation of the bouncing bed phase does not depend on the initial layout of particles.

4. Granular damping from non-spherical particles in the bouncing bed phase

In the interests of conciseness, this section focuses on important trends in the damping efficiency results but does not present every result obtained. The full dataset is available online [54] and can be consulted to verify the applicability of the conclusions made.

4.1. Effect of particle shape on granular energy dissipation

In Fig. 10, the experimentally measured damping efficiency curves for particles $\alpha = 0.70$, 1.00 and 1.50 are shown at different frequencies for both gravity-to-vibration orientations. As mentioned before, the peak amplitude of each curve corresponds to the onset of the bouncing bed motional phase, Γ_{optimum}.

Fig. 10 shows that maximum achievable efficiency is relatively insensitive to particle aspect ratio, excitation orientation, and frequency, being in the range 0.75–0.85. Note that this applies for all particle shapes considered in this work. Also, for spherical particles, the bouncing bed onset occurs at the amplitudes anticipated using Eqs. (12) and (13). However, it can be seen that the non-spherical particles considerably increase the bouncing bed onset amplitude regardless of vibration frequency and excitation orientation. The prolate type ($\alpha = 1.50$) achieves the bouncing bed at slightly higher amplitudes than the oblate type ($\alpha = 0.70$), but they are close to each other when compared with the perfectly spherical particles. This similarity may be because both particle types have nearly the same sphericity level despite their shapes, i.e., the sphericity is around 0.977 for $\alpha = 0.70$ and 0.973 for $\alpha = 1.50$.

Fig. 10 indicates two important outcomes that directly affect the practical design of a granular damper. First, if a damper is designed to operate around the bouncing bed onset amplitude assuming perfectly spherical particles, the damper performance can dramatically decrease if the shape deviates from being a perfect sphere as the optimum occurs at a higher amplitude. Secondly, if there

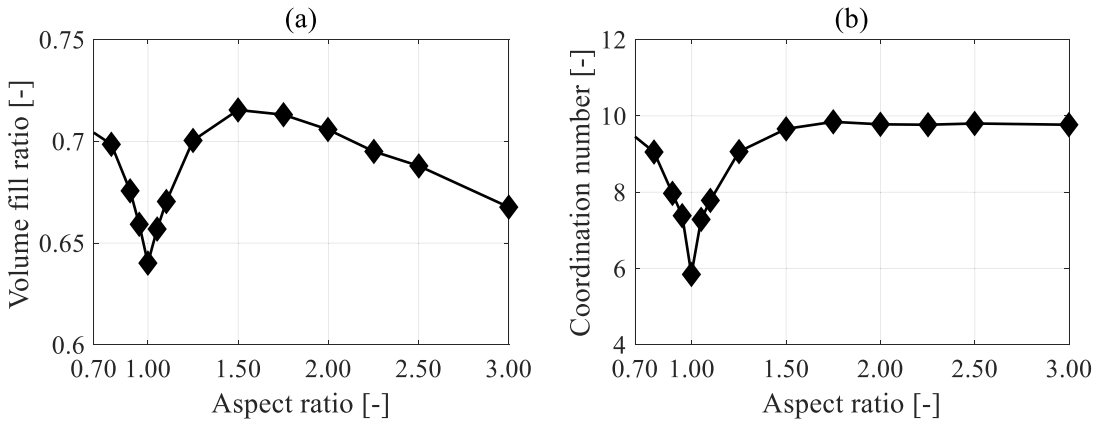

Fig. 12. Static granular medium properties under random close packing condition [55]: (a) volume fill ratio and (b) coordination number.

is a length restriction in the design space such that the bouncing bed onset cannot be achieved under the anticipated operating conditions, the situation can be addressed by employing non-spherical particles. This can be clearly seen from the damping efficiency results of $\Gamma > 8$ at 20 Hz and $\Gamma > 30$ at 40 Hz in Fig. 10.

4.2. Influence of particle shape on the bouncing bed onset amplitude

The sensitivity to particle aspect ratio of the bouncing bed onset amplitude $\Gamma_{optimum}$ is shown for both experimental and DEM data in Fig. 11(a) and (b). Precise values were obtained from curves fitted to the datapoints (as discussed earlier with regard to Fig. 9(d)). It is apparent from these figures that the experimental and numerical results indicate a consistent trend with respect to aspect ratio regardless of frequency or vibration-to-gravity orientation. The experimental $\Gamma_{optimum}$ vs aspect ratio plots have two apparent zones: a v-shaped trough between $\alpha = 0.70$ and $\alpha = 1.50$ with an obvious minimum around $\alpha = 1.00$ (perfect sphere); and an approximately constant value between $\alpha = 1.50$ and $\alpha = 3.00$. Additionally, the left edge of v-shape ($\alpha = 0.70$) has similar bouncing bed onset amplitude to that in the constant zone ($\alpha = 1.50$ to $\alpha = 3.00$). This shows that $\Gamma_{optimum}$ is shifted to higher amplitudes by introducing non-spherical particles, however the level of this amplitude shift becomes relatively insensitive to aspect ratio for $\alpha >= 1.5$. It can be also seen that the simulation results agree with physical measurements.

At high amplitudes, (when $\Gamma > \Gamma_{optimum}$) the rate at which the damping efficiency reduces with amplitude is not significantly affected by particle aspect ratio, as can be seen in Fig. 10. The damping efficiency at a specific amplitude in this zone is therefore an indicator of the proximity to $\Gamma_{optimum}$. This can be seen in the similarity of the curves for damping efficiency at a fixed amplitude (Fig. 11(c) and(d)) to those for $\Gamma_{optimum}$ (Fig. 11(a) and (b)). This was found to be consistent for all other amplitudes considered.

4.3. Explanation for the shift in onset amplitude

The upward shift in $\Gamma_{optimum}$ that was observed when particle sphericity was reduced, has two probable causes which are discussed briefly below.

I. Some spheroidal particles pack together more closely than perfect spheres. For the same number of particles within the damper cavity, this creates a larger apparent clearance which results in a higher $\Gamma_{optimum}$ as indicated by Eq. (12). For example, Donev et al. [55] show that when $\alpha = 1.50$ the maximum random packing ratio is 0.71 while it is 0.64 for $\alpha = 1.00$. The denser particle bed takes up less space resulting in an increase in clearance which in turn indicates an increase in $\Gamma_{optimum}$ of approximately 18%. However, as can be seen in Fig. 11(a), the increase in $\Gamma_{optimum}$ for this condition was over 50% indicating at least one additional cause for the shift.

II. Spheroidal particles are likely to create a granular medium that is more resistant to shear deformation because in comparison to perfect spheres, spheroids have less freedom to rotate and translate within the block of particles as the granular medium is deformed. In the bouncing bed onset zone (around $\Gamma_{optimum}$) significant local shear deformation of the bed takes place during the collisions with the end walls. This means that the vibrational intensity required to achieve this behaviour needs to be higher when sphericity reduces.

The work of Donev et al. on the properties of granular media under static loading [55] provides support for the explanations given above. Fig. 12(a) shows the maximum volume fill ratios that they found for various randomly packed spheroid particles. For these maximum fill conditions, the associated coordination numbers, described as the mean number of contacts for a single particle, are presented in Fig. 12(b).

The packing ratio of a granular medium (or inversely the porosity) correlates with its overall stiffness and therefore the effective

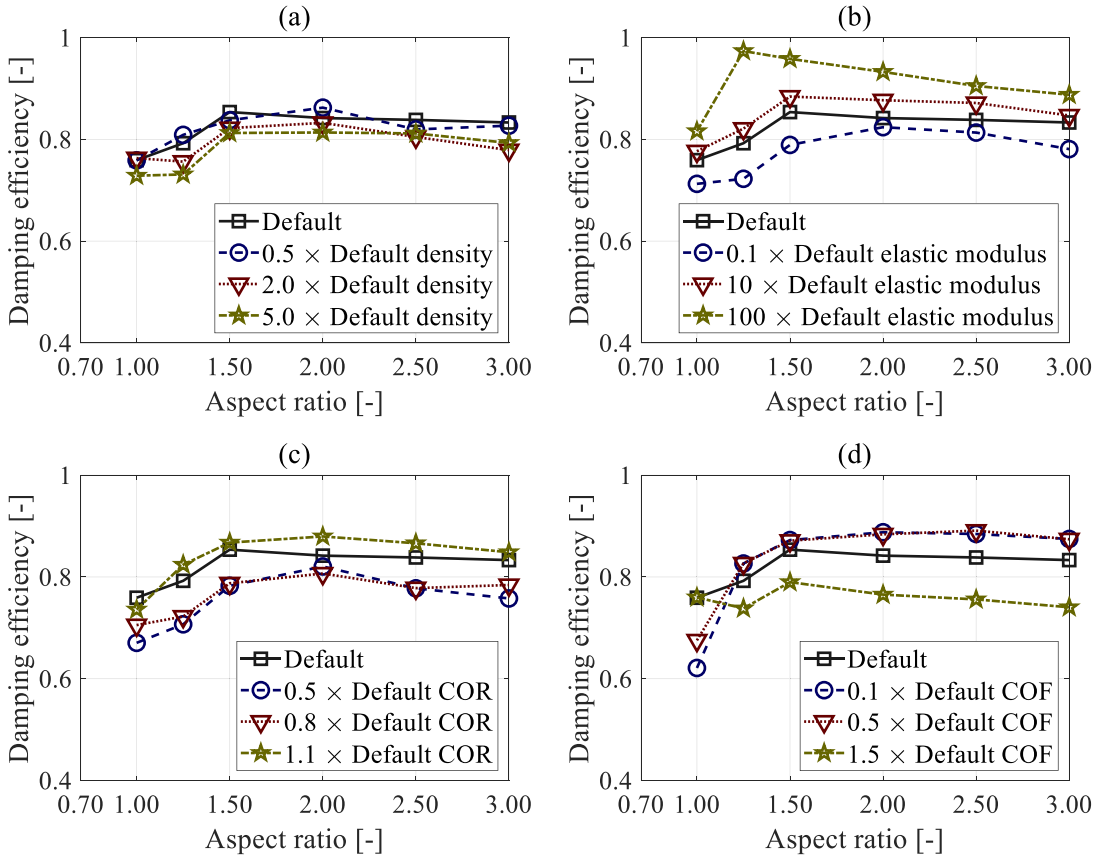

Fig. 13. Sensitivity analysis of granular damping efficiency for $\Gamma = 35$ horizontal excitation at 40 Hz to: (a) density, (b) elastic modulus, (c) COR and (d) COF.

elastic modulus [56]. Thus, Fig. 12(a) indicates that the overall stiffness is lowest for perfect spheres, reaches a maximum for intermediate aspect ratio and then reduces again at high aspect ratios (confirmed elsewhere in the literature [56]). However, the effect of aspect ratio on the ability to resist shear loads is different. The shear stiffness is related to the coordination number [57] which is presented in Fig. 12(b). Perfect spheres still provide the lowest stiffness against shear loads. However, rather than displaying a reduction in the shear stiffness at high aspect ratios, it can be seen that values for $\alpha = 1.50$ and $\alpha = 3.00$ are approximately the same. This behaviour is consistent with the observed shift characteristic in the bouncing bed onset amplitude $\Gamma_{optimum}$ in Fig. 11, highlighting the significance of shear stiffness in this motional phase.

4.4. Sensitivity to contact and material properties

The material and contact properties shown in Table 1 were used throughout the investigations reported in this paper. As there is evidence in the literature that material properties can affect granular damping levels [28,29], it was considered important to check the generality of the understanding developed around the effects of aspect ratio. For this reason, a sensitivity analysis was conducted for the investigated damper utilising DEM simulations.

The sensitivity study considered the effects of large changes in density, elastic modulus, coefficient of restitution (COR) and coefficient of friction (COF). A single excitation condition (horizontal vibrations at 40 Hz with $\Gamma = 35$) was considered appropriate as it resulted in the bouncing bed motional behaviour for all conditions. By selecting an excitation intensity that was higher than the bouncing bed onset amplitude $\Gamma_{optimum}$ it was possible to represent changes to $\Gamma_{optimum}$ using the damping efficiency – as was discussed in Section 4.2 when considering Fig. 11.

Results of the sensitivity study are set out in Fig. 13 in a similar way to the results presented in Fig. 11(c) and (d). It should be noted that because the sensitivity analysis is based on DEM simulations, it was possible to observe only the behaviour on right side of v-shaped feature i.e., $\alpha \geq 1.00$.

Fig. 13(a) shows that an increase in the density of the particle material causes a slight reduction in the granular damping efficiency and this change is consistent for all particle aspect ratios. As the particle mass effect is removed by comparing the damping efficiency results, the slight reduction in efficiency may relate to changes in the deformation of the bed during each collision event caused by their increased intensity.

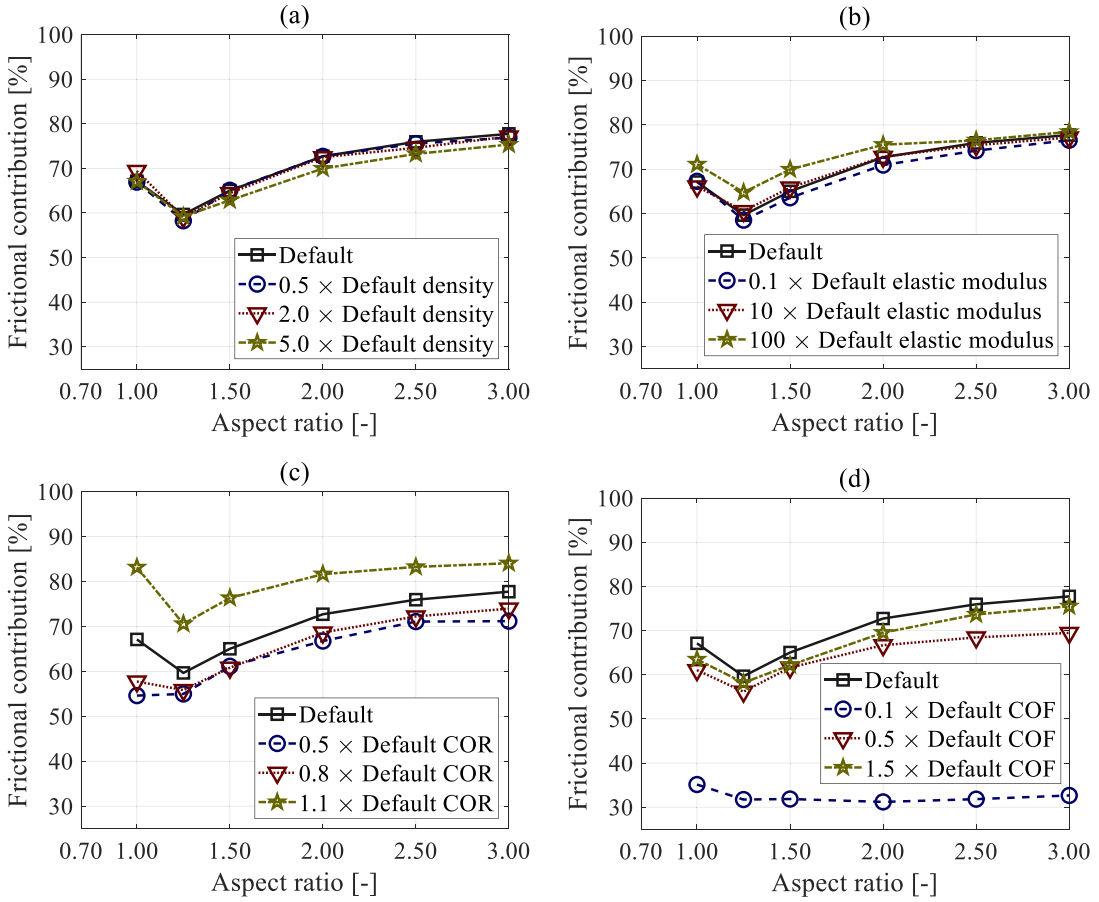

Fig. 14. Fraction of energy dissipation *via* sliding friction, showing sensitivity to: (a) density, (b) elastic modulus, (c) COR and (d) COF.

Fig. 13(b) and (c) shows that harder (higher elastic modulus) or lower loss (higher COR) material provides slightly higher damping efficiency irrespective of particle aspect ratio. Particles with higher modulus or COR result in a less dense particle bed because less energy is lost in individual inter-particle impacts reducing their tendency to collect tightly together. A looser particle bed deforms more, dissipating more energy during each collision event.

Unlike the other properties investigated, COF significantly changes the ratio of shear stiffness to axial stiffness of the particle bed, which is similar to what the particle shape does, as discussed before. As a result, its variation has a significant effect on the dissipation efficiency curves, as can be seen in Fig. 13(d). Decreasing the COF increases sensitivity to particle shape as can be seen by the increased difference in damping efficiency between $\alpha = 1.00$ to $\alpha = 1.50$. The most likely explanation for this is that COF plays a similar role to particle aspect ratio in the way it links the shear stiffness of the particle bed to its normal stiffness, albeit at a much smaller physical scale.

Sliding friction is usually the dominant energy dissipation mechanism in granular dampers [58]. In the bouncing bed motional phase, collisions with the end walls involve significant sliding in particle-particle and particle-wall contacts. The fraction of energy dissipation attributed to sliding friction for all the conditions presented in Fig. 13 are provided in Fig. 14. Note that the remaining dissipation arises from inelastic collision.

In Fig. 14, it can be seen that energy dissipation is dominated by frictional interactions in the bouncing bed phase, and the importance of friction tends to increase as the aspect ratio increases. Density and elastic modulus do not affect this behaviour significantly. The effect of the COR is only significant if it is large (i.e., low internal loss in the particles means friction becomes more important), and the effect of the COF is only significant if it is small (i.e., low sliding friction means that more dissipation is lost in impacts). This tendency of friction and impact mechanisms to compensate for each other has been noted previously [59]. It is interesting to note that the lowest frictional contribution occurs consistently when the aspect ratio $\alpha = 1.25$ although the reason for this is not clear.

5. Conclusions

This paper has reported the results of the first combined experimental-DEM study on granular dampers containing non-spherical

particles. It has shown that particle shape has a clear influence on the energy dissipation behaviour of granular dampers operating in the bouncing bed phase. Reducing sphericity moves the optimum condition, known as the bouncing bed onset, to a higher excitation amplitude. It has been shown that this effect is closely related to the ease with which the granular medium deforms in shear and a correlation has been noted with the coordination number, which is the mean number of contacts per particle. The changes caused by particle shape are insensitive to particle stiffness, density and coefficient of restitution. However, the particle coefficient of friction plays a similar role to particle shape at a smaller scale. Overall, the results provide a reliable guide to the designer for exploiting the efficient energy dissipation nature of bouncing bed phase.

Declaration of Competing Interest

The authors declare that they have no competing interest.

Data availability

Data will be made available on request.

Acknowledgment

The first author would like to acknowledge the support from the Turkish Ministry of National Education by providing the scholarship.

References

[1] H.V. Panossian, Structural damping enhancement *via* non-obstructive particle damping technique, J. Vib. Acoust. 114 (1992) 101–105, https://doi.org/10.1115/1.2930221.
[2] Z. Xu, M.Yu Wang, T. Chen, A particle damper for vibration and noise reduction, J. Sound Vib. 270 (2004) 1033–1040, https://doi.org/10.1016/S0022-460X(03)00503-0.
[3] B.M. Shah, D. Pillet, X.M. Bai, L.M. Keer, Q. Jane Wang, R.Q. Snurr, Construction and characterization of a particle-based thrust damping system, J. Sound Vib. 326 (2009) 489–502, https://doi.org/10.1016/j.jsv.2009.06.007.
[4] P. Veeramuthuvel, K.K. Sairajan, K. Shankar, Vibration suppression of printed circuit boards using an external particle damper, J. Sound Vib. 366 (2016) 98–116, https://doi.org/10.1016/j.jsv.2015.12.034.
[5] F. Duvigneau, S. Koch, E. Woschke, U. Gabbert, An effective vibration reduction concept for automotive applications based on granular-filled cavities, J. Vib. Control. 24 (2018) 73–82, https://doi.org/10.1177/1077546316632932.
[6] S. Koch, F. Duvigneau, R. Orszulik, U. Gabbert, E. Woschke, Partial filling of a honeycomb structure by granular materials for vibration and noise reduction, J. Sound Vib. 393 (2017) 30–40, https://doi.org/10.1016/j.jsv.2016.11.024.
[7] Z. Lu, Z. Wang, S.F. Masri, X. Lu, Particle impact dampers: past, present, and future, Struct. Control Heal. Monit. 25 (2018) 1–25, https://doi.org/10.1002/stc.2058.
[8] L. Gagnon, M. Morandini, G.L. Ghiringhelli, A review of particle damping modeling and testing, J. Sound Vib. 459 (2019), 114865, https://doi.org/10.1016/j.jsv.2019.114865.
[9] R.D. Friend, V.K. Kinra, Particle impact damping, J. Sound Vib. 233 (2000) 93–118, https://doi.org/10.1006/jsvi.1999.2795.
[10] K. Mao, M.Y. Wang, Z. Xu, T. Chen, DEM simulation of particle damping, Powder Technol. 142 (2004) 154–165, https://doi.org/10.1016/j.powtec.2004.04.031.
[11] W. Liu, G.R. Tomlinson, J.A. Rongong, The dynamic characterisation of disk geometry particle dampers, J. Sound Vib. 280 (2005) 849–861, https://doi.org/10.1016/j.jsv.2003.12.047.
[12] N. Ahmad, R. Ranganath, A. Ghosal, Modeling and experimental study of a honeycomb beam filled with damping particles, J. Sound Vib. 391 (2017) 20–34, https://doi.org/10.1016/j.jsv.2016.11.011.
[13] M.Y. Yang, Development of Master Design Curves For Particle Impact Dampers, The Pennsylvania State University, 2003.
[14] C.X. Wong, M.C. Daniel, J.A. Rongong, Energy dissipation prediction of particle dampers, J. Sound Vib. 319 (2009) 91–118, https://doi.org/10.1016/j.jsv.2008.06.027.
[15] Y. Duan, Q. Chen, Simulation and experimental investigation on dissipative properties of particle dampers, J. Vib. Control. 17 (2011) 777–788, https://doi.org/10.1177/1077546309356183.
[16] M. Ben Romdhane, N. Bouhaddi, M. Trigui, E. Foltête, M. Haddar, The loss factor experimental characterisation of the non-obstructive particles damping approach, Mech. Syst. Signal Process. 38 (2013) 585–600, https://doi.org/10.1016/j.ymssp.2013.02.006.
[17] C. Salueña, T. Pöschel, S.E. Esipov, Dissipative properties of vibrated granular materials, Phys. Rev. E 59 (1999) 4422–4425, https://doi.org/10.1103/PhysRevE.59.4422.
[18] A. Sack, M. Heckel, J.E. Kollmer, F. Zimber, T. Pöschel, Energy dissipation in driven granular matter in the absence of gravity, Phys. Rev. Lett. 111 (2013) 1–5, https://doi.org/10.1103/PhysRevLett.111.018001.
[19] A. Sack, K. Windows-Yule, M. Heckel, D. Werner, T. Pöschel, Granular dampers in microgravity: sharp transition between modes of operation, Granul. Matter. 22 (2020) 1–6, https://doi.org/10.1007/s10035-020-01017-x.
[20] P. Eshuis, K. van der Weele, D. van der Meer, R. Bos, D. Lohse, Phase diagram of vertically shaken granular matter, Phys. Fluids 19 (2007), https://doi.org/10.1063/1.2815745.
[21] G.H. Ristow, Critical exponents for granular phase transitions, Europhys. Lett. 40 (1997) 625–630, https://doi.org/10.1209/epl/i1997-00514-3.
[22] K. Zhang, T. Chen, X. Wang, J. Fang, Rheology behavior and optimal damping effect of granular particles in a non-obstructive particle damper, J. Sound Vib. 364 (2016) 30–43, https://doi.org/10.1016/j.jsv.2015.11.006.
[23] Z. Yin, F. Su, H. Zhang, Investigation of the energy dissipation of different rheology behaviors in a non-obstructive particle damper, Powder Technol. 321 (2017) 270–275, https://doi.org/10.1016/j.powtec.2017.07.090.
[24] N. Meyer, R. Seifried, Toward a design methodology for particle dampers by analyzing their energy dissipation, Comput. Part. Mech. (2020), https://doi.org/10.1007/s40571-020-00363-0.
[25] F. Terzioglu, J.A. Rongong, C.E. Lord, Motional phase maps for estimating the effectiveness of granular dampers, Mech. Syst. Signal Process. 188 (2023), 110038, https://doi.org/10.1016/j.ymssp.2022.110038.

[26] N. Popplewell, M. Liao, A simple design procedure for optimum impact dampers, J. Sound Vib. 146 (1991) 519–526, https://doi.org/10.1016/0022-460X(91)90707-Q.
[27] K.S. Marhadi, V.K. Kinra, Particle impact damping: effect of mass ratio, material, and shape, J. Sound Vib. 283 (2005) 433–448, https://doi.org/10.1016/j.jsv.2004.04.013.
[28] Z. Lu, X. Lu, S.F. Masri, Studies of the performance of particle dampers under dynamic loads, J. Sound Vib. 329 (2010) 5415–5433, https://doi.org/10.1016/j.jsv.2010.06.027.
[29] Z. Lu, S.F. Masri, X. Lu, Parametric studies of the performance of particle dampers under harmonic excitation, Struct. Control Heal. Monit. 18 (2011) 79–98, https://doi.org/10.1002/stc.359.
[30] M. Sánchez, C.M. Carlevaro, L.A. Pugnaloni, Effect of particle shape and fragmentation on the response of particle dampers, J. Vib. Control 20 (2014) 1846–1854, https://doi.org/10.1177/1077546313480544.
[31] J.M. Bajkowski, B. Dyniewicz, C.I. Bajer, Damping properties of a beam with vacuum-packed granular damper, J. Sound Vib. 341 (2015) 74–85, https://doi.org/10.1016/j.jsv.2014.12.036.
[32] H. Pourtavakoli, E.J.R. Parteli, T. Pöschel, Granular dampers: does particle shape matter? New J. Phys. 18 (2016) https://doi.org/10.1088/1367-2630/18/7/073049.
[33] F. Terzioglu, J.A. Rongong, C.E. Lord, The dissipative characteristics of oblate particles in granular dampers, in: Proceedings of the 6th International Conference on Structural Dynamics, EURODYN, 2020, pp. 4851–4866, https://doi.org/10.47964/1120.9393.20452.
[34] M. Saeki, Impact damping with granular materials in a horizontally vibrating system, J. Sound Vib. 251 (2002) 153–161, https://doi.org/10.1006/jsvi.2001.3985.
[35] M. Saeki, Analytical study of multi-particle damping, J. Sound Vib. 281 (2005) 1133–1144, https://doi.org/10.1016/j.jsv.2004.02.034.
[36] M. Pasha, C. Hare, M. Ghadiri, A. Gunadi, P.M. Piccione, Effect of particle shape on flow in discrete element method simulation of a rotary batch seed coater, Powder Technol. 296 (2016) 29–36, https://doi.org/10.1016/j.powtec.2015.10.055.
[37] M. Alizadeh, A. Hassanpour, M. Pasha, M. Ghadiri, A. Bayly, The effect of particle shape on predicted segregation in binary powder mixtures, Powder Technol. 319 (2017) 313–322, https://doi.org/10.1016/j.powtec.2017.06.059.
[38] P. Parafiniuk, M. Molenda, J. Horabik, Influence of particle shape and sample width on uniaxial compression of assembly of prolate spheroids examined by discrete element method, Phys. A Stat. Mech. Appl. 416 (2014) 279–289, https://doi.org/10.1016/j.physa.2014.08.063.
[39] D. Markauskas, R. Kačianauskas, A. Džiugys, R. Navakas, Investigation of adequacy of multi-sphere approximation of elliptical particles for DEM simulations, Granul. Matter. 12 (2010) 107–123, https://doi.org/10.1007/s10035-009-0158-y.
[40] V. Angelidakis, S. Nadimi, M. Otsubo, S. Utili, CLUMP: a code library to generate universal multi-sphere particles, SoftwareX 15 (2021), 100735, https://doi.org/10.1016/j.softx.2021.100735.
[41] Altair Engineering Inc., EDEM 2021.1, (2021).
[42] F. Terzioglu, J.A. Rongong, C.E. Lord, The effect of particle surface roughness on granular energy dissipation performance, in: Proceedings of the 24th International Congress on Acoustics, Gyeongju, South Korea, 2022. https://eprints.whiterose.ac.uk/194344/.
[43] M. Masmoudi, S. Job, M.S. Abbes, I. Tawfiq, M. Haddar, Experimental and numerical investigations of dissipation mechanisms in particle dampers, Granul. Matter. 18 (2016) 1–11, https://doi.org/10.1007/s10035-016-0667-4.
[44] M.Y. Yang, G.A. Lesieutre, S.A. Hambric, G.H. Koopmann, Development of a design curve for particle impact dampers, Smart Struct. Mater. (2004) 450, https://doi.org/10.1117/12.540019, 2004 Damping Isol., Bellingham, WA.
[45] P.A. Cundall, O.D.L. Strack, A discrete numerical model for granular assemblies, Geotechnique 29 (1979) 47–65, https://doi.org/10.1680/geot.1979.29.1.47.
[46] S.E. Olson, An analytical particle damping model, J. Sound Vib. 264 (2003) 1155–1166, https://doi.org/10.1016/S0022-460X(02)01388-3.
[47] K.L. Johnson, Contact Mechanics, First, Cambridge University Press, New York, 1985.
[48] A. Di Renzo, F.P. Di Maio, Comparison of contact-force models for the simulation of collisions in DEM-based granular flow codes, Chem. Eng. Sci. 59 (2004) 525–541, https://doi.org/10.1016/j.ces.2003.09.037.
[49] W.J. Stronge, Impact Mechanics, Second, Cambridge University Press, New York, 2018.
[50] J. Coaplen, W.J. Stronge, B. Ravani, Work equivalent composite coefficient of restitution, Int. J. Impact Eng. 30 (2004) 581–591, https://doi.org/10.1016/j.ijimpeng.2003.10.038.
[51] S. Bin Yeom, E. Ha, M. Kim, S.H. Jeong, S.J. Hwang, D.H. Choi, Application of the discrete element method for manufacturing process simulation in the pharmaceutical industry, Pharmaceutics 11 (2019), https://doi.org/10.3390/pharmaceutics11080414.
[52] Y. Tsuji, T. Tanaka, T. Ishida, Lagrangian numerical simulation of plug flow of cohesionless particles in a horizontal pipe, Powder Technol. 71 (1992) 239–250, https://doi.org/10.1016/0032-5910(92)88030-L.
[53] M.N. Bannerman, J.E. Kollmer, A. Sack, M. Heckel, P. Mueller, T. Pöschel, Movers and shakers: granular damping in microgravity, Phys. Rev. E 84 (2011) 1–9, https://doi.org/10.1103/PhysRevE.84.011301.
[54] F. Terzioglu, J. Rongong, C. Lord, Experimental and simulation damping efficiency results of a granular damper, for various particle aspect ratios, (2023). 10.15131/shef.data.21931647.
[55] A. Donev, I. Cisse, D. Sachs, E.A. Variano, F.H. Stillinger, R. Connelly, S. Torquato, P.M. Chaikin, Improving the density of jammed disordered packings using ellipsoids, Science 303 (2004) 990–993, https://doi.org/10.1126/science.1093010, 80-.
[56] J. Wiacek, M. Molenda, J. Horabik, J.Y. Ooi, Influence of grain shape and intergranular friction on material behavior in uniaxial compression: experimental and DEM modeling, Powder Technol. 217 (2012) 435–442, https://doi.org/10.1016/j.powtec.2011.10.060.
[57] E. Azéma, F. Radjai, F. Dubois, Packings of irregular polyhedral particles: strength, structure, and effects of angularity, Phys. Rev. E Stat. Nonlinear Soft Matter Phys. 87 (2013) 1–14, https://doi.org/10.1103/PhysRevE.87.062203.
[58] F. Terzioglu, J.A. Rongong, C.E. Lord, Construction of motional phase maps for granular dampers, in: INTER-NOISE and NOISE-CON CongreSS AND CONFERENCE Proceedings 265, 2023, pp. 128–139, https://doi.org/10.3397/IN_2022_0025.
[59] B. Darabi, J.A. Rongong, Polymeric particle dampers under steady-state vertical vibrations, J. Sound Vib. 331 (2012) 3304–3316, https://doi.org/10.1016/j.jsv.2012.03.005.